ACS Energy LETTERS

http://pubs.acs.org/journal/aelccp

LETTER

Strain Engineering: Reduction of Microstrain at the Perovskite Surface via Alkali Metal Chloride Treatment Enhances Stability

Do-Kyoung Lee,[#] Kostas Fykouras,[#] Tim Kodalle, Raphael F. Moral, Craig P. Schwartz, Nobumichi Tamura,* Keith V. Lawler,* Linn Leppert,* and Carolin M. Sutter-Fella*

Cite This: *ACS Energy Lett.* 2025, 10, 1039−1049

Read Online

ACCESS | Metrics & More | Article Recommendations | Supporting Information

ABSTRACT: **Degradation of halide perovskites under a humid atmosphere is the major challenge preventing widespread commercial deployment of this material class. Here it is shown that strain engineering via alkali metal chloride treatment at the $FAPbI_3/SnO_2$ interface effectively improves moisture-related stability. CsCl and KCl treatments reduce microstrain at the perovskite surface and slow the α- to δ-phase transformation. Alkali metal treatments with LiCl, NaCl, and RbCl led to an increase in microstrain and faster degradation. The compressive strain at the perovskite surface was the smallest for CsCl and was linked to improved stability. First-principles density functional theory calculations confirm the preferential formation of alkali defects at interstitial positions at the perovskite surface. Particularly CsCl and KCl treatments lead to a release of compressive strain at the perovskite surface and local structural distortions that may favor passivation of surface defects. In contrast, the room-temperature dynamics of Li interstitials result in an overall expansion of lattice volume, which may be linked to more facile lattice degradation.**

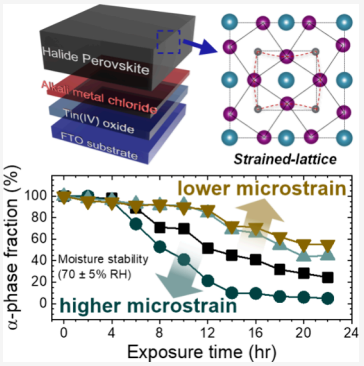

Organic−inorganic metal halide perovskite materials have been spotlighted as a promising candidate for photovoltaic devices as well as facilitating various optoelectronic applications thanks to their exceptional properties.[1−4] The biggest challenge for halide perovskites is instability under operational and environmental conditions. This is related to the nature of the soft crystal lattice of halide perovskites with ionic bonds and low defect formation energies.[5,6] Due to their hygroscopic and ionic nature, they are exceedingly sensitive to moisture and oxygen. Multiple strategies are being explored to enhance the long-term stability of halide perovskite solar cells. Two promising directions are strain engineering and interface stabilization.[7−11]

Strain can manifest as microstrain, compressive/tensile strain, and atomic displacement vectors.[7] Microstrain reflects the inhomogeneous deformation of lattice planes and contributions from local regions that are under compressive or tensile strain. It can be defined as the average localized variation of strain in the material, resulting in X-ray diffraction peak broadening. Microstrain, which is influenced by several factors, such as phase transitions, grain boundaries, and misfits on the atomic scale, is one of the major origins of reducing the phase stability of halide perovskite materials. Kim et al. reported on microstrain relaxation through the incorporation of small amounts of cesium and methylenediammonium in $FAPbI_3$ (FA = formamidinium) and associated it with a decrease in trap concentration as well as superior thermal stability.[8] Additives that are not incorporated into the lattice have also been reported to reduce the microstrain.[12] In addition, it was reported that local lattice strain can induce the formation of point defects and these were linked to being a major degradation source.[13] It was also shown that atomic vacancies exhibit a significant affinity for oxygen and water molecules accelerating degradation.[13,14] Molecular dynamics simulations of $CsPbI_3$ show that iodine vacancies and interstitials are mobile and negatively affect stability.[15] Suppressing vacancy formation by increasing their defect formation energy was demonstrated to enhance stability.[13] Lastly, microstrain at the perovskite/vacuum interface is expected to lead to compressive strain in the bonds perpendicular to the surface even in a pristine material without defects as shown by DFT calculations.[16]

Contrarily, strain across the whole film such as tensile or compressive strain can originate from differences in thermal

Received: December 2, 2024
Revised: January 12, 2025
Accepted: January 21, 2025
Published: February 3, 2025

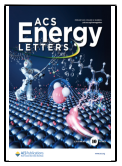

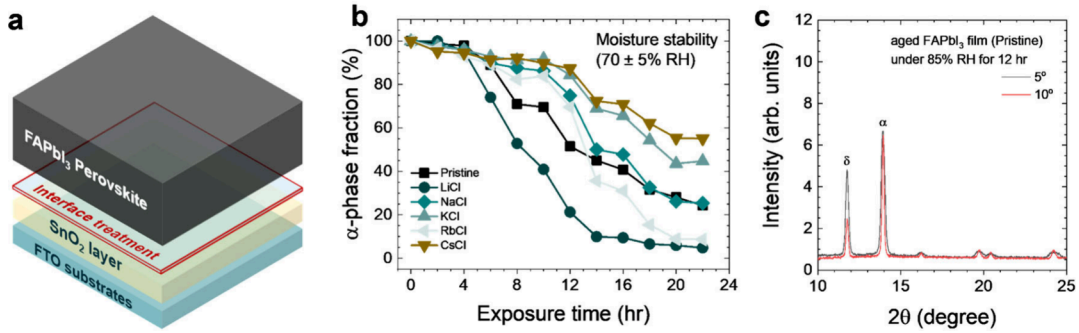

Figure 1. Phase stability of halide perovskites with interface treatments. (a) Illustration of sample configuration where $FAPbI_3$ halide perovskite films were deposited on FTO/SnO_2 substrates treated with alkali metal chloride salts. (b) Moisture stability of the α-phase $FAPbI_3$ fraction over time with various alkali metal chloride treatments extracted from XRD measurements. (c) XRD patterns for aged $FAPbI_3$ films taken at 5° and 10° incidence angles.

expansion coefficients and/or a lattice mismatch between the perovskite film and the substrate. Zhao et al. found the compressive strain in the out-of-plane direction and the tensile strain in the in-plane direction are related to the thermal expansion coefficient mismatch between the perovskite material and substrate.[9] This lattice strain was found to be correlated with perovskite instability and a decrease in the ion migration activation energy. To effectively manage strain as a phase stabilization strategy, a better understanding of microstrain as well as out-of-plane and in-plane strain in halide perovskite thin films is needed. A strategy to improve long-term stability via interface stabilization by modifying relevant layers and interfaces was presented by Liu et al.[11] To stabilize the SnO_2/perovskite interface, they used ethylenediaminetetraacetic acid dipotassium (EDTAK) salt treated at the interface to tune the energetic alignment at the SnO_2/perovskite interface. The use of this salt has several effects, mitigating the reaction of OH^- in a commercial SnO_2 solution and making use of the passivation effect of K^+. KCl was also demonstrated to suppress unwanted recombination at the SnO_2/perovskite interface, to eliminate hysteresis, and to increase the solar cell's open-circuit voltage.[17]

Here, we report on the effects of alkali metal chloride treatment at the SnO_2/perovskite interface and its ability to regulate lattice strain and thus improve the halide perovskite stability. We find a strain gradient from the perovskite surface to the SnO_2/perovskite interface with a transition from more compressive to tensile, respectively. Both, CsCl and KCl treatments lead to superior moisture stability compared to the reference. It is shown that the microstrain at the perovskite surface is significantly reduced for CsCl and KCl treatments, while the other alkali metal chloride treatments increase the microstrain, leading to faster α- to δ-phase transformation under environmental conditions, especially humidity. As degradation initiates at the perovskite surface, we link the improved moisture stability in the cases of CsCl and KCl treatments with beneficial strain and defect engineering. First-principles density functional theory (DFT) calculations confirm the preferential formation of alkali defects at the perovskite-vacuum interface at interstitial sites. By using machine-learned interatomic force fields to explore the room-temperature dynamics of these interstitial defects, we found that Cs and K incorporation leads to compressive strain release and large local structural distortions that may point to enhanced defect passivation, while the dynamics of Li interstitials do not distort the on-average cubic lattice but result in an overall expansion of lattice volume, which may be linked to more facile lattice degradation.

To investigate the effect of alkali metal chlorides on the intrinsic stability of perovskite thin films, we prepared $FAPbI_3$ films on FTO/SnO_2 substrates with and without an alkali metal chloride treatment. The treatment was directly applied to the surface of the SnO_2 layer (Figure 1a) using a spin coating method by depositing a 20 or 100 mM coating solution of alkali metal chloride dissolved in deionized water followed by annealing at 150 °C for 30 min under ambient atmosphere. After cooling down, the substrates were immediately transferred to a N_2-filled glovebox (see Materials and Methods section for more details).

Upon exposure to external environmental stressors (inert N_2, 70% relative humidity (RH), 1-sun illumination, and 150 °C) we tracked the X-ray diffraction (XRD) patterns over exposure time, as can be seen in Supplementary Figures S1–S3. The comparison of phase stability under these different stressors reveals that 100 mM LiCl treatment leads to a significant reduction in the α-phase $FAPbI_3$ stability. While none of the alkali chloride treatments led to improved phase stability compared to the reference sample under inert N_2, one sun illumination, and 150 °C stressors, a clear difference was found in moisture stability. Figure 1b shows the α-phase $FAPbI_3$ fraction calculated from XRD over time under exposure to 70 ± 5% RH. While LiCl, NaCl, and RbCl treatments lead to poor moisture stability, KCl and CsCl treatments improve the stability of $FAPbI_3$ compared to the pristine case. To assess whether degradation of halide perovskites starts at the perovskite surface or the bulk/SnO_2 interface, XRD measurements were carried out with 5° and 10° incidence angles, where the 5° measurement is slightly more surface sensitive. The integrated diffraction peak for the δ-phase at 2θ = 12.6° is higher at the lower incidence angle, indicating that the degradation processes occur from the surface of the perovskite film as seen in Figure 1c and Supplementary Figure S4. Although the treated alkali metal chloride interlayer is sandwiched between the perovskite and SnO_2 contact, degradation appears to originate from the surface, and its rate depends on the alkali metal. Since the existence of both the alkali metal cation and the chlorine counteranion could affect the phase stability, we performed X-ray photoelectron spectroscopy (XPS) measurements on the perovskite surface with and without alkali metal chloride treatments. Neither of the samples show clear signatures of the alkali metals nor Cl (Supplementary Figures S5 and S6). Only

https://doi.org/10.1021/acsenergylett.4c03334
ACS Energy Lett. 2025, 10, 1039−1049

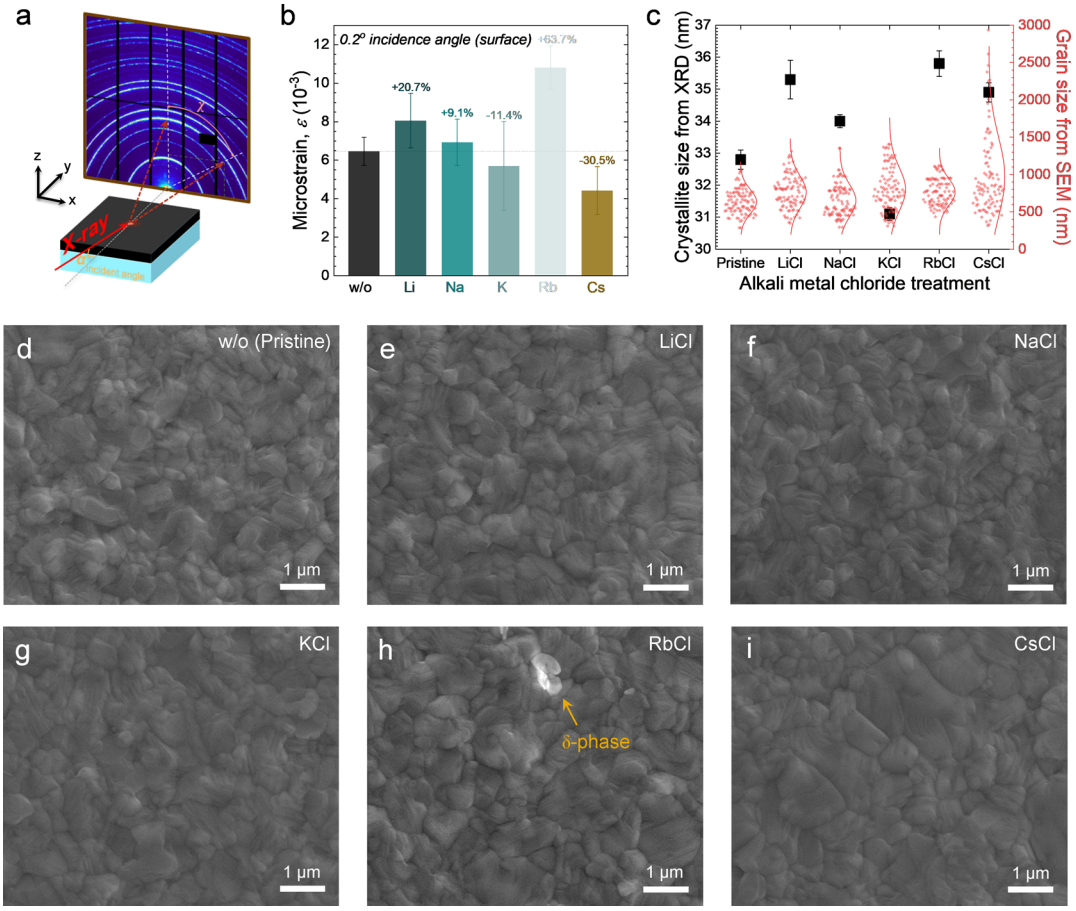

Figure 2. Lattice strain at the perovskite surface. (a) Schematic of a synchrotron-based grazing-incidence wide-angle X-ray scattering (GIWAXS) measurement. χ is the azimuthal angle with a basis at 0° angle in relation to the q_z axis along the out-of-plane direction. (b) Calculated microstrain (ε) extracted by using the Williamson-Hall equation from samples prepared with 20 mM alkali metal chloride treatments. (c) Crystallite size extracted from Scherrer analysis and average grain sizes manually extracted from the top-view scanning electron microscopy (SEM) images for perovskite films (d) without and with (e) LiCl, (f) NaCl, (g) KCl, (h) RbCl, and (i) CsCl treatments. For the distribution of the grain sizes, analysis was performed on 100 individual grains, and a normal distribution curve was added to the data.

for high CsCl concentrations (100 mM), there is a notable Cs signal indicating that Cs is present during $FAPbI_3$ fabrication and diffuses to the perovskite surface. Noting that the XPS detection limits are typically between 0.1−1.0 atomic percent, there are likely small amounts of alkali metals and/or chlorine that accumulate at the perovskite surface but are not detected.[18] Previous studies using a similar alkali metal treatment as presented here found that the alkali metal chlorides are preferentially located between the charge transport and the perovskite layer.[17,19] Alternatively, alkali metal halides have been directly used as perovskite precursor additives and scanning transmission electron microscopy−energy dispersive X-ray spectroscopy (STEM-EDX) showed alkali metal accumulation at the top and bottom surfaces as well as at grain boundaries.[20] In a control experiment to investigate if the alkali metals possibly diffuse toward the $FAPbI_3$ surface, an about five times thinner perovskite film was deposited onto the FTO/SnO_2/alkali metal chloride treated stack. XPS measurements were then taken from the surfaces of the FTO/SnO_2/interlayer/$FAPbI_3$ stacks (Supplementary Figure S7). There are small XPS 'bumps'of each alkali metal species for the thinner perovskite film conditions, this is indicative of the possibility of alkali metal species diffusion during the film formation processes. In agreement with previous literature, alkali metal species might be mostly distributed at interfaces between SnO_2 and halide perovskite layer and grain boundaries (Supplementary Figures S6, S7). Moreover, to further verify the possibility of alkali metal chloride diffusion into the halide perovskite layer during growth, and consequently a modification of the crystallization kinetics, we performed in-situ photoluminescence (PL) and grazing-incidence wide-angle X-ray scattering (GIWAXS) measurements. There are no notable differences in the crystallization kinetics for the $FAPbI_3$ films during the spin coating or annealing processes (Supplementary Figures S8−10). Therefore, based on these findings and in agreement with previous literature, we assume that the alkali metal chloride layer is mostly located at the bulk/SnO_2 interface, i.e. at the position where it was deposited.

In order to evaluate the residual lattice strain for different alkali metal chloride treatments, we conducted synchrotron-based GIWAXS measurements in a reflection geometry (Figure 2a). Following our observation that degradation occurred from the perovskite surface, we measured GIWAXS below the critical incidence angle (~0.2°) to extract the lattice parameters of the surface of the perovskite film with an estimated X-ray penetration depth around 10−30 nm (see calculated X-ray attenuation length in Figure S11). In Figure

https://doi.org/10.1021/acsenergylett.4c03334
ACS Energy Lett. 2025, 10, 1039−1049

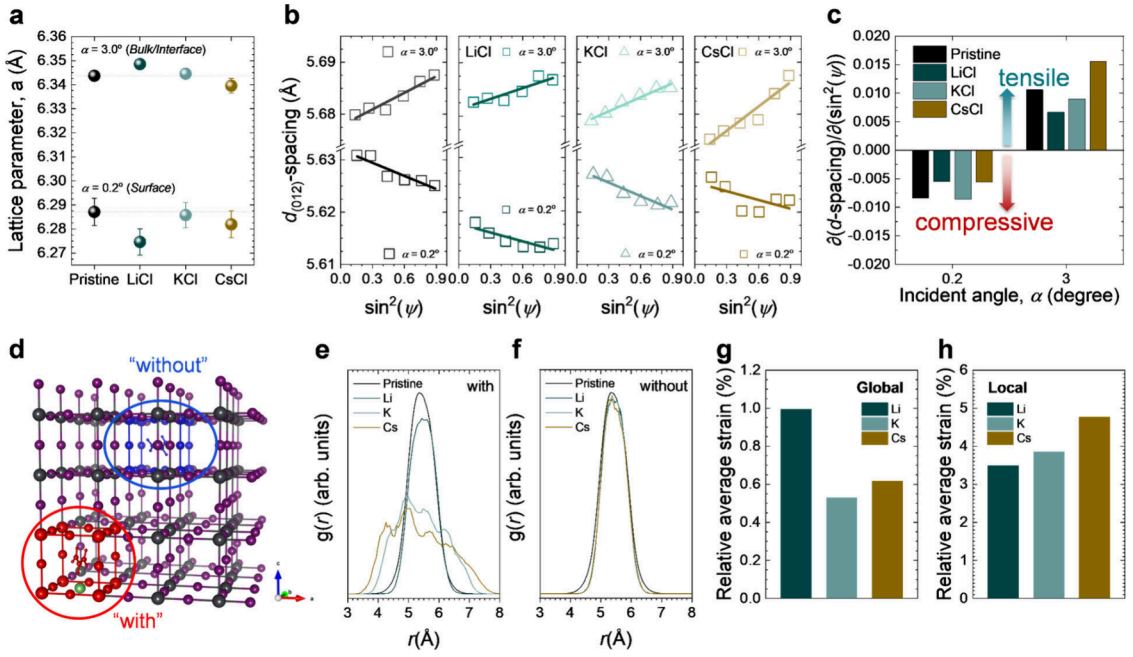

Figure 3. Depth-dependent lattice deformation. Lattice parameters were obtained from GIWAXS Bragg peaks measured with (a) 0.2° and 3.0° incidence angles. Note that the calculated lattice parameters with error bars represent four different crystal planes, i.e., (002), (012), (022), and (222). (b) *d*-Spacing versus $\sin^2(\psi)$ plot for the (012) plane, where GIWAXS was measured with 0.2° and 3.0° incidence angles. (c) Linear slope extracted from $(\partial(d_{(012)})/\partial(\sin^2(\psi))$ with negative slope representing compressive and positive slope representing tensile strain. (d) Definition of the subunits "with" (red) and "without" (blue) alkali defect (marked in green) in the 4 × 4 × 4 supercells used for molecular dynamics simulations. Gray spheres represent Pb and purple spheres I atoms. For clarity, FA molecules are shown only in the red and blue sublattices and omitted from the rest of the structure. Pair distribution function (PDF) of FA to the next-nearest Pb for subunits "with" (e) and "without" (f) defects for Cs, K and Li. Relative global (g) and local (h) strains with respect to pristine sample, as defined in the main text.

2b, the microstrain (ε) at the surface was extracted from the slope of the curves based on the Bragg peak width using the Williamson-Hall equation (Figures S12, S13, more information in the Materials and Methods section). The microstrain values for KCl (= 5.78×10^{-3}) and CsCl (= 4.53×10^{-3}) are roughly 10 and 30% lower than that for the pristine sample ($\varepsilon_{pristine}$ = 6.52×10^{-3}), respectively, while LiCl, NaCl, and RbCl exhibit higher microstrain (Figure 2b). RbCl (= 10.67×10^{-3}) and LiCl (= 7.87×10^{-3}) show the highest microstrain compared to the pristine sample while exhibiting the lowest stability. We hypothesized that the different magnitudes of the residual strain are related to alkali metal species localized in crystal lattices and size effects where small atoms increase and large atoms decrease the surface microstrain. This conclusion is supported by our first-principles calculations, as detailed below. However, it remains unclear why Rb does not follow the overall size trend predicted by our calculations. We note that two independent syntheses, degradation, and strain measurements resulted in the same findings (see the change in microstrain for 20 and 100 mM treatments in Supplemental Figure S14).

Top-view scanning electron microscopy (SEM) images (Figure 2d–i) do not show significant differences in morphology, with the CsCl-treated sample showing a slightly enlarged apparent grain size.[3,21,22] To compare the apparent grain size of halide perovskite films for each condition, we estimated the grain size distribution and calculated the crystallite size based on manual analysis of grooves visible in the SEM images and Scherrer analysis of the GIWAXS patterns (Figure 2c and Supplemental Figure S15), respectively. As can be seen in Figure 2c and Supplementary Figure S15, CsCl-treated halide perovskite films exhibit a higher average grain size of around 967 nm compared to other conditions while also featuring many small grains. While top-view SEM images do provide information on morphology, they do not provide crystallographic information. What appears as grooves representing the intersection of grain boundaries visible in the SEM may not reveal the subgrain structure.[23,24] While the average grain size is the lowest for the pristine and highest for the CsCl-treated sample, there is no difference in crystallite size (Figure 2c). Thus, we expect minor effects of grain boundaries and microstructure on the strain evolution. Notably, the sample with RbCl treatment shows the δ-phase, illustrating the lower sample stability and possibly explaining its large microstrain.

Given the observations that the KCl- and CsCl-treated samples show improved stability and reduced microstrain at the perovskite surface, while LiCl treatment results in the worst stability, we will mostly focus on the former in the following sections and measure depth-dependent GIWAXS. With increasing incidence angle, i.e., when moving from the perovskite surface to the SnO_2/perovskite interface region, the lattice parameters a are increased for all samples (pristine, LiCl, KCl, and CsCl conditions) from ~6.285 Å (Surface-dominant, incidence angle α = 0.2°) to ~6.345 Å (bulk interface-dominant, incidence angle α = 3°), as seen in Figure 3a. The lattice parameters for the CsCl-treated sample at both incidence angles are slightly smaller than for the pristine, while the changes in those values for the KCl-treated sample are negligible. These results indicate that Cs induces more compressive strain with out-of-plane direction than K at both the surface and bulk interface, potentially resulting in lower

https://doi.org/10.1021/acsenergylett.4c03334
ACS Energy Lett. 2025, 10, 1039−1049

microstrain and improved phase stability of the CsCl-treated halide perovskite film. For the LiCl-treated sample, the surface lattice parameter is compressed, and the bulk interface lattice is expanded compared to the pristine sample. We anticipated that the larger variation between lattice parameters for the surface and bulk interface can possibly induce higher inhomogeneous lattice strain distribution and/or lattice distortion, resulting in higher microstrain and poor phase stability due to destabilizing crystal structure. The bulk interface-dominant lattice parameters (i.e., incidence angle $\alpha = 3°$) are in line with the results from our molecular dynamics (MD) simulations showing a slightly increased lattice parameter for the LiCl-treated sample as discussed below.

Next, the residual compressive/tensile in-plane strain is estimated from the linear slope $\partial(d)/\partial(\sin^2(\psi))$ for the (012) crystal plane (see Materials and Methods section). In general, $\sin^2(\psi)$ and d show a linear relationship, and the slope of the linear fit represents the magnitude of the in-plane strain.[25] A positive slope indicates tensile in-plane strain and a negative slope, compressive in-plane strain. Figure 3b shows the d-spacing as a function of $\sin^2\psi$ at 0.2° and 3.0° X-ray incidence angles, and Figure 3c depicts their derivatives. All samples show compressive in-plane strain at the perovskite surface and tensile in-plane strain at the SnO_2/perovskite interface, indicating a strain crossover within the film. The most notable difference is the lower compressive surface strain and almost 50% higher tensile strain at the SnO_2/perovskite interface when CsCl treatment was applied. In contrast, KCl treatment can induce less in-plane tensile strain at the bulk interface and slightly more in-plane compressive strain at the surface than the pristine sample as well as the CsCl-treated sample, resulting in lower microstrain and enhanced phase stability. To further clarify our hypothesis for the KCl and CsCl conditions, we also calculated the $\partial(d)/\partial(\sin^2(\psi))$ linear slope values for the (002) plane as can be seen in Supplementary Figure S16. Supplementary Figure S16a demonstrates the more enhanced compressive strain with in-plane direction for the KCl-treated sample compared to the pristine and CsCl samples, which is in good agreement with the in-plane lattice strain results for the (012) plane. Therefore, we propose that the improved phase stability of the halide perovskite films is predominantly affected by compressive strain for CsCl- and KCl-treated samples, respectively.

A previous report on $(FAPbI_3)_{0.85}(MAPbBr_3)_{0.15}$ has shown that the tensile strain increases toward the perovskite film surface.[26] Transmission electron microscopy confirmed a lattice constant increase from the bottom to the surface, and it was explained from time-of-flight secondary ion mass spectrometry (TOF-SIMS) depth profiles that this is correlated to a composition gradient over the film thickness. It was found that the MA^+ fragment decreased from the surface to the bulk. Compressive surface strain is in line with first-principles DFT calculations for pristine surfaces,[16] but may additionally be affected by surface reconstruction, dangling bonds, or adsorption of species. The crossover to tensile strain in the samples treated with alkali metal chlorides may be related to the preference of alkali metal atoms to occupy interstitial positions, as predicted by our first-principles calculations, leading to a lattice expansion. Other reasons for this observation include a change in microstructure over the film thickness and phenomena related to the thin film growth process. Our synthesis follows a typical antisolvent process, where it is possible that crystallization starts from the surface, where rapid supersaturation is induced by the antisolvent and fast solvent evaporation at the film surface occurs.

To gain an atomistic understanding of the incorporation of alkali metals into the perovskite lattice, we performed first-principles density functional theory (DFT) calculations (see Materials and Methods). These calculations, carried out for 2 × 2 × 2 supercells with randomly oriented FA molecules and using the PBE-D3(BJ) functional as implemented in QuantumEspresso, show similar results to those of Cao et al.,[27] where A-site substitutions of alkali cations are in general more favorable than interstitial additions (see Supplementary Figure S17). The only favorable defect found was the substitution of Cs for an FA at the A-site, and the favorability of an A-site substitution decreased with decreasing the alkali ionic radius. The defect formation energies of an interstitial addition here are similar to those of Cao et al.,[27] however these show a reversed trend of Li being less favorable than Cs that we attribute to the changes in interaction strengths and optimized lattices from the inclusion of dispersion interactions in our work. The B-site substitutions calculated here are not as unfavorable as reported in Cao et al., which we again attribute to the inclusion of dispersion interactions, as our changes in optimized volumes are smaller than reported in that study. To further investigate alkali defect formation at the perovskite/vacuum interface, we constructed a 2 × 2 × 5 slab model with both possible surface terminations of $FAPbI_3$, i.e., PbI_2 and FAI (see Supplementary Table T1 and Supplementary Figure S18). In these calculations, we probed size effects by inserting Li, Na, K, and Cs into interstitial window sites (i.e., the vacant center of a PbI_2 face of a cubic α-phase unit cell of $FAPbI_3$), substituting FA at A-sites, and substituting Pb at B-sites at both interfaces and in the bulk. As expected, we found that the favorability of an A-site substitution of FA in the bulk increases with increased alkali atomic size, as the larger alkali atoms can maximize interactions with neighboring iodine atoms. A-site substitution of Cs in the bulk and at the PbI_2/vacuum interface are the only substitutions found with a favorable negative defect formation energy with the bulk being the preferred site.[28] The most favorable site for an A-site substitution of K is at the PbI_2/vacuum interface, and for Na and Li it is at the FAI/vacuum interface. As opposed to the supercell calculations, the addition of an interstitial alkali atom in a window site in the bulk becomes more favorable with decreasing atomic radius due to strain effects as the x and y dimensions of the slabs were fixed. The most favorable site for Na, K, and Cs insertion is at the PbI_2/vacuum interface, with alkali atoms tending to protrude into the vacuum, suggesting alkali metal enrichment at the perovskite/vacuum interface. For Li, a bulk insertion is slightly more favorable than at the PbI_2/vacuum interface, and this is due to Li moving off the center of the window to strengthen its interaction with three of the neighboring iodines. Additionally, these static calculations show that interstitial alkali defects lead to lattice expansion while A-site substitutional defects lead to lattice compression, as expected based on their atomic radii.

Since we expect additional effects due to temperature-induced dynamic disorder and alkali atom migration, we further carried out molecular dynamics simulations based on machine-learned interatomic force fields as implemented in VASP, trained on-the-fly on DFT-PBE-D3 energies, forces and stress tensors.[29] These molecular dynamics simulations were run on 4 × 4 × 4 supercells at 300 K. Further details can be found in the Methods Section. We chose the interstitial

https://doi.org/10.1021/acsenergylett.4c03334
ACS Energy Lett. 2025, 10, 1039−1049

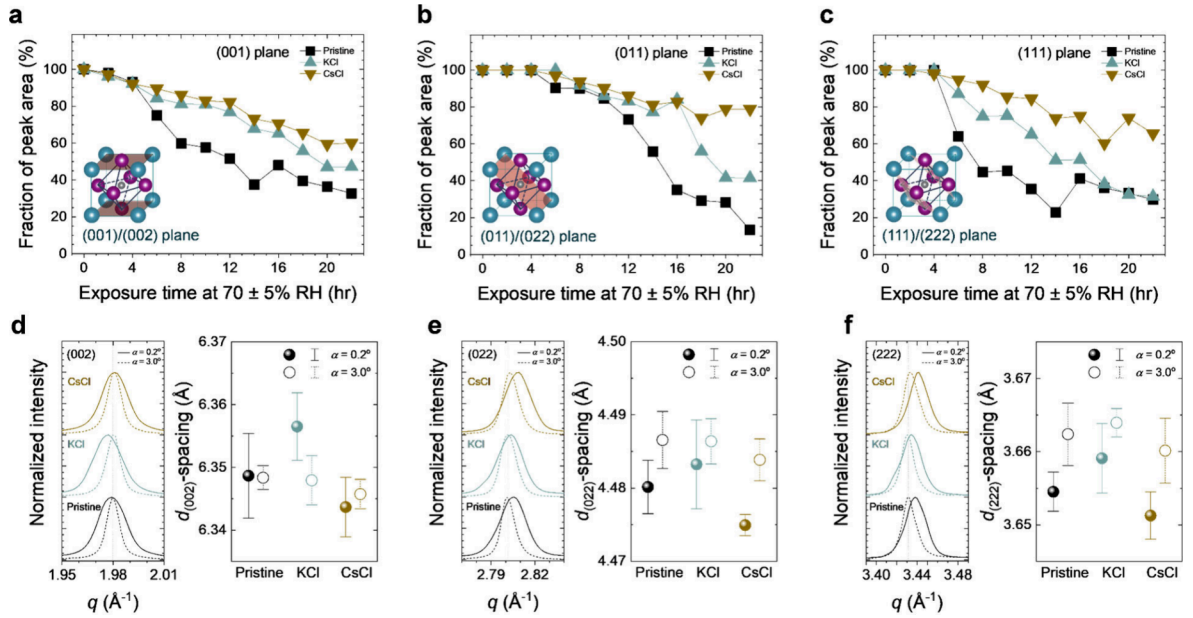

Figure 4. Crystal plane-dependent degradation. (a−c) Moisture stability of α-phase $FAPbI_3$ corresponding to (a) (001), (b) (011), and (c) (111) crystal planes as a function of exposure time to 70 ± 5% relative humidity. The fraction of peak area along various crystal planes was calculated by using the [(h k l) for α-phase $FAPbI_3$]/[(010) for δ-phase $FAPbI_3$)] ratio. Diffraction peaks (left) and *d*-spacing values corresponding to (d) (002), (e) (022), and (f) (222) crystal planes obtained from synchrotron-based GIWAXS. GIWAXS measurements were performed at 0.2° (surface) and 3.0° (bulk) incidence angles with ±40° χ integration range.

window site as the starting point for these calculations, running calculations for Li, K, Rb, and Cs. For analysis of the results, we defined two subunits in our 4 × 4 × 4 supercells, corresponding to the unit cell containing the interstitial defect atom ("with") and a unit cell as far as possible away from the defect atom ("without") as shown in Figure 3d. We calculated the pair distribution function (PDF) of FA to its next-nearest Pb neighbors in both unit cells as a measure for local structural distortions induced by the defect atom (Figure 3e and f). For all three alkali atoms, we found that the PDF of the unit cell without the defect is similar to that of the pristine system (Figure 3f), suggesting minimal local distortions away from the defect atom. In contrast, we found that the local structural distortions in the unit cells with the defect atom are significantly different (Figure 3e), where the local structural distortion is decreased with a decreasing alkali atom size. Furthermore, we estimated the local lattice strain by comparing the volume of the unit cell with the defect atom and the formula-unit volume of the pristine system (Figure 3g and h). As expected based on atomic size, the largest local strain is observed for Cs followed by K and Li. Notably, the global supercell strain (Figure 3g) is significantly larger for Li than for Cs and K due to the larger volume of the Li-containing supercell, which is a consequence of the larger-amplitude thermal motion of Li. On average, we found that Li resides close to the center of the interstitial window site with large displacements primarily along the diagonal of the window plane as shown in Supplementary Figure S19. K and Cs move further away from the window plane, with Cs moving furthest toward the center of the unit cell, pushing away FA. This finding is in line with the larger probability for Cs to substitute FA as compared to other alkali halides (Supplementary Figure S17), and suggests a potential pathway for FA vacancy passivation that might contribute to enhanced stability in the presence of Cs. Note that Rb follows the expected atomic-size dependent trends in our calculations (Figure S20).

Correlated with our experimental observation that the surface microstrain is changing in samples with alkali metal chloride treatment, we assumed that the different magnitudes of residual compressive strain are related to alkali metal concentration and size effects. We hypothesized that the reduced surface microstrain observed for CsCl and KCl treatments positively affects the α-phase stability. Furthermore, our calculations suggest that Cs and K tend to migrate out of the window site toward the A-site position and that A-site substitution is energetically favorable for these alkali atoms at the perovskite/vacuum interface. In combination, these mechanisms may lead to the passivation of surface defects such as FA vacancies, which can act as seeds for surface degradation and δ-phase formation.[30]

To further elucidate the possible correlation between phase stability and residual strain, we investigated crystal plane-dependent moisture stability along the (001), (011), and (111) planes for different alkali metal chloride treatments (Figure 4a−c). Degradation occurs independently of the crystal plane for the reference film but most severely in the (011) plane. CsCl and KCl outperform the reference and, interestingly, CsCl exhibits superior moisture stability along the (011) plane where the XRD peak fraction drops to 80% compared to <20% for the reference. Since degradation was found to propagate from the surface (Figure 1c), we next analyzed the *d*-spacing differences at the surface and the SnO_2/perovskite interface (Figure 4d−f). The GIWAXS patterns used for this analysis show random crystal orientation (full ring patterns, Supplementary Figure S21). Thus, we also analyzed the *d*-spacing variation for out-of-plane (i.e., χ = 0° filled circles) and in-plane (i.e., χ = 40° open circles) directions at the perovskite film surface (incidence angle = 0.2°), as can be seen in Supplementary Figure S22. Neither of these analyses shows a clear trend, leading to the assumption that the reduction in surface microstrain might contribute the most to the observed stability enhancement for CsCl and KCl

https://doi.org/10.1021/acsenergylett.4c03334
ACS Energy Lett. 2025, 10, 1039−1049

treatments, as discussed above. A study by Zheng et al. reports on anisotropic lattice strain in the (111) plane that drives the α- to δ-phase transformation.[31] In particular, alloying $FAPbI_3$ with MABr was found to lead to lattice contraction and significantly improved stability under humid conditions. These observations align with the average positions and thermal ellipsoids extracted from our MD simulations (see Figure S19). The results show that Li predominantly remains within the (001) plane. Its thermal ellipsoid features a long principal axis along the diagonal of the (001) plane, indicating significant thermal motion within that plane. In contrast, Cs migrates from the window site toward the tetrahedral site, with the long principal axis of its thermal ellipsoid oriented in the (011) plane, suggesting preferential thermal motion along that direction.

We have investigated the effect of alkali metal chloride treatment at the SnO_2/perovskite interface on stability and strain in $FAPbI_3$ thin films. The α- to δ-phase transformation under humid conditions initiates from the surface and is significantly slowed for KCl and CsCl treatments, while these treatments also lead to a reduction in surface microstrain. On the contrary, other alkali metal treatments (LiCl, NaCl, RbCl) lead to an increase in surface microstrain and a faster α- to δ-phase transformation. Since microstrain reflects inhomogeneous deformation of lattice planes and contributions from local regions that are compressively or tensilely strained, it is suggested that CsCl and KCl treatments reduce lattice deformations. In-depth analysis of synchrotron-based X-ray diffraction data revealed a crossover from tensile to compressive strain when moving from the perovskite/SnO_2 interface to the surface of the film. The observed compressive surface strain is possibly reduced through CsCl and KCl treatments. DFT calculations confirm the preferential formation of alkali defects at the perovskite/vacuum interface. We attribute the effect of these alkali atom defects on microstrain and surface stability to a combination of size effects, thermal motion of interstitial alkali atoms, and concentration gradients. Poor stability observed for LiCl treatment may be linked to the dynamics of Li interstitials leading to an overall lattice volume expansion as probed by machine-learned interatomic force fields. This study rationalizes strain engineering via alkali metal treatments to improve stability by altering surface microstrain.

MATERIALS AND METHODS

Formamidinium iodide (FAI) and methylammonium chloride (MACl) were purchased from Greatcell Solar Materials. Lead(II) iodide (99.99%, trace metal basis, for perovskite precursor) was purchased from TCI Chemicals. Lithium chloride (LiCl, ≥99.98%, trace metals basis), sodium chloride (NaCl, ≥99.0%), potassium chloride (KCl, 99.0−100.5%), rubidium chloride (RbCl, 99.8%, trace metals basis), cesium chloride (CsCl, ≥99.999%, trace metals basis), *N*,*N*-dimethylformamide (DMF, 99.8%, anhydrous), dimethyl sulfoxide (DMSO, 99.9%, anhydrous), and diethyl ether (contains 1 ppm BHT as inhibitor, anhydrous, ≥99.7%) were purchased from Sigma-Aldrich. SnO_2 solution (tin(IV) oxide, 15% in H_2O colloidal dispersion) was purchased from Alfa Aesar. All chemicals were used as received without any further purifications.

Preparation of $FAPbI_3$ Perovskite Precursor Solution. The $FAPbI_3$ perovskite solution was prepared with FAI (1.5 M), PbI_2 (1.5 M), and MACl (0.225 M) precursors dissolved in 1 mL of mixed DMF/DMSO solvent (DMF:DMSO = 4:1 volume ratio). To fully dissolve precursors in the solvent, the solution was vigorously shaken at room temperature. The perovskite precursor solution was filtered through PTFE filters with 0.2 μm pore size before use.

Formation of $FAPbI_3$ Perovskite Films. The FTO substrates were cleaned with detergent solution, acetone, deionized water, and ethanol for min subsequently by sonication. The cleaned FTO substrates were dried with nitrogen gas and then treated by UV/Ozone cleaner for 60 min. The diluted SnO_2 solution (4 wt % in deionized water) was loaded onto the cleaned FTO substrate, and then spun at 3000 rpm for 30 s. The SnO_2-deposited substrates were heated at 150 °C for 30 min on a hot plate. Before coating the alkali metal chloride solution, the FTO/SnO_2 substrates were treated with UV/Ozone cleaner for 60 min. To prepare alkali metal chloride solutions, LiCl, NaCl, KCl, RbCl, and CsCl were dissolved in deionized water with 20 mM and 100 mM concentrations. The alkali metal chloride treatments were deposited onto UV/Ozone-treated FTO/SnO_2 substrates by spin-coating at 3000 rpm for 30 s and then heated at 150 °C for 30 min. After cooling down, the substrates were immediately transferred to the N_2-filled glovebox. The $FAPbI_3$ perovskite layer was deposited on the FTO/SnO_2 substrate with alkali metal chloride treatment via spin coat deposition at 1000 rpm for 10 s with 200 rpm/s and 5000 rpm for 40 s with 2000 rpm/s. 200 μL of chlorobenzene as an antisolvent was dropped onto the spinning substrate at 5 s prior to the end of the spin coating process. The as-coated film was annealed at 60 °C for 6 min and 150 °C for 20 min on the hot plate under a N_2 atmosphere.

Film Characterization. Laboratory-based X-ray diffraction (XRD) measurements were performed by using a Bruker D8-Discover with Co−Kα X-ray radiation operating at 35 kV and 40 mA. For the environmental stability tests, this instrument was used to follow the α phase evolution. During measurement, the sample stage was moving over a 2 × 2 mm^2 area. 2θ values in XRD patterns for Co−Kα (λ = 0.17890 nm) were converted to that for Cu−Kα (λ = 0.15406 nm). X-ray photoelectron spectroscopy (XPS) was performed using a Kratos Axis DLD X-ray photoelectron spectroscopy system with a monochromated Al−Kα (1486.6 eV) X-ray beam source. The samples were measured in the dark under a pressure of 10^{-8} Torr without a charge neutralizer. Scanning electron microscopy (SEM) images were measured using Zeiss Gemini Ultra-55 Analytical SEM instrument with 10 kV accelerating voltage.

Synchrotron-Based GIWAXS Data Collection and Analysis. GIWAXS measurements were taken at beamline 12.3.2 of the Advanced Light Source.[32] The incidence angle of the incoming X-ray beam was set to 0.2° and 3° with a beam energy of 10 keV. The sample detector distance (SDD) was set to 155 mm, and the detector was positioned at an angle of 35° from the sample plane. The GIWAXS data were recorded with an integration time of one s using a Pilatus 1 M 2D detector (Dectris Ltd.). The beam footprint is about 5 μm × 500 μm at 0.2° and 5 μm × 38 μm at 3°. The error bar for 500 μm is about ±200 μm due to the shallow angle.

Lattice parameter analysis was done by fitting Voigt profiles to the respective diffraction peaks and making use of Bragg's law equation: $n\lambda = 2d\sin\theta$ to convert the peak positions to d spacing. One standard deviation of the fitted peak position was used to estimate the uncertainty of the lattice parameter

https://doi.org/10.1021/acsenergylett.4c03334
ACS Energy Lett. 2025, 10, 1039−1049

measurements and transformed to d-spacing using Gaussian error propagation.

Lattice parameter calculation for cubic structure is based on

$$\frac{1}{d^2} = \frac{k^2}{a^2} + \frac{l^2}{b^2} + \frac{m^2}{c^2} = \frac{(k^2 + l^2 + m^2)}{a^2}$$

(for cubic, a = b = c)

$$a = \sqrt{d^2(k^2 + l^2 + m^2)}$$

First, bare FTO peaks were measured at different incidence angles (α) with 0.2, 0.5, 1.0, and 3.0 degrees, then, the FTO peak position was compared with the FTO position measured in the FTO/SnO_2/alkali metal chloride/perovskite stack taken at different incidence angles. This comparison shows offsets of $-1.84 \times 10^{-3} \pm 6.05 \times 10^{-4}$ for $\alpha = 1°$ and $-0.53 \times 10^{-3} \pm 5.05 \times 10^{-4}$ for $\alpha = 3°$. Based on that the offset for the 0.2° data was approximated because this surface sensitive measurement does not show FTO peaks.

Williamson-Hall analysis was used to calculate the microstrain ε extracted from the slope:[33]

$$\beta\cos\theta = 4\varepsilon\sin\theta + (K\lambda/D)$$

where β is fwhm, K is a constant value depending on peak shape (0.91−1.0), λ is the wavelength of the incident beam, D is the crystallite size, and θ is the Bragg angle. A shape factor K = 0.94 was used here in agreement with previous reports on halide perovskites for approximately spherical crystal shape.[34,35] We integrated the diffraction peaks with a wide χ angle range of ±40° to quantitatively compare the microstrain distribution in the entire film.

The XRD-sin2ψ technique was applied following the previous report to determine residual stress.[25] In this method, the residual stress value is determined through a linear relationship between sin2ψ and the experimentally measured diffraction angle (2θ)

$$d_{\phi\psi} = \left[\left(\frac{1+\nu}{E}\right)\sin^2\psi - \left(\frac{2\nu}{E}\right)\right]\cdot\sigma\cdot d_0 + d_0$$

where E is Young's modulus, ν is Poisson's ratio, σ is a residual stress/strain component, d_0 is interplanar lattice spacing for strain-free crystals, ψ is the angle between the surface normal vector of the sample and the bisector of X-ray incidence angle.[36] Based on this equation, the residual compressive/tensile strain in a material can be quantitatively estimated from the linear slope $\partial(d)/\partial(\sin^2(\psi))$.

Scherrer analysis was performed based on integrated GIWAXS data for the (002) reflex. The X-ray wavelength was 0.124 nm and the shape factor K was assumed as 0.9 for the cubic crystallites observed in SEM. Measured fwhm values were corrected for beam divergence (0.0017 nm) and the energy bandwidth (0.0001 nm) according to the previous report by Sidhik et al.[37]

Calculations/MD Simulations. Plane-wave Density Functional Theory (DFT) structural optimizations were performed with Quantum Espresso[38,39] using the PBE functional[40] with the -D3 dispersion correction[41] with Becke-Johnson (BJ) damping.[42] The SSSP PBE Efficiency v.1.3.0 pseudopotentials[43] were used with a 60 Ry cutoff for the wave functions, a 240 Ry cutoff for the charge density, and Gaussian smearing with a 0.005 Ry width. The initial guesses for the 2 × 2 × 2 supercells and 2 × 2 × 5 slabs (with 15 Å of vacuum in the c direction) have randomly rotationally oriented FA ions in every unit cell of lattice constant 6.3943 Å; that lattice constant was found by optimizing several orientations of FA ions in single cubic cells with an initial guess of the previously reported PBEsol[44] lattice constant of 6.3613 Å.[45] A 10^{-8} Ry SCF cutoff, a 10^{-3} au force cutoff, and a 3 × 3 × 3 k-grid were used for the supercell optimizations. The larger slab optimizations used a 10^{-7} Ry SCF cutoff, a 7×10^{-3} au force cutoff, and a 2 × 2 × 1 k-grid.

Molecular Dynamics (MD) simulations were performed with the Vienna-Ab-Initio Simulation Package (VASP)[46−48] using a plane wave basis and projector augmented wave (PAW) pseudopotentials.[49] We used the PBE functional[40] with the -D3 dispersion corrections as above for all calculations.[38] To accelerate the MD simulations, machine-learned force fields were trained on the fly[29] using the Gaussian approximation potential[50] with two- and three-body atomic descriptors based on the smooth overlap of atomic orbitals (SOAP) method.[51] For all studied systems the training of the force fields was performed on a 2 × 2 × 2 supercell of $FAPbI_3$ where for the systems containing defects, the defect was placed at an interstitial window site at the start of the training. The electronic minimization was performed using a 400 eV plane wave cutoff energy and a 4 × 4 × 4 k-point grid. For all systems the force fields were trained for 100 ps at a temperature of 400 K. The force fields were then used in production mode on a 4 × 4 × 4 supercell for all studied systems under isothermal and isobaric NPT conditions at 300 K for 120 ps. The parameters used for the control of the isothermal and isobaric conditions were the same as in ref 52. The mean squared displacement for the cases of Cs, K and Li is shown in Figure S23 where the expected size trend is observed with Li moving the most in the lattice followed by K and then Cs. In Supplementary Figure S24 the evolution of the lattice parameters throughout the MD simulation is shown, where the calculated values are in good agreement with the experimental lattice parameters showing the validity of the force fields. While for the systems containing Cs, K and Li, we observe a cubic phase, the lattice parameters of the system with Rb correspond to a tetragonal phase, which may originate from the hopping of Rb between interstitial window sites, contrary to expectations based on size effects. All results shown in this paper were obtained by averaging over 4 different MD runs for each alkali metal, except for the calculation of the thermal ellipsoids, where only 1 MD run was chosen. We excluded an initial equilibration period of 2 ps for the analysis of these MD runs.

■ ASSOCIATED CONTENT

Data Availability Statement

All the relevant data are available from the corresponding authors upon request.

Supporting Information

The Supporting Information is available free of charge at https://pubs.acs.org/doi/10.1021/acsenergylett.4c03334.

XRD measurements and fits; XPS spectra; SEM images; in situ PL contour plots; in situ GIWAXS contour plots; Williamson-Hall fit data; grain size histograms; defect formation energy histogram and table; anisotropic displacement parameters; pair distribution function; mean squared displacement plots and lattice parameters (PDF)

https://doi.org/10.1021/acsenergylett.4c03334
ACS Energy Lett. 2025, 10, 1039−1049

AUTHOR INFORMATION

Corresponding Authors

Nobumichi Tamura − *Advanced Light Source, Lawrence Berkeley National Laboratory, Berkeley, California 94710, United States*; Email: ntamura@lbl.gov

Keith V. Lawler − *Nevada Extreme Conditions Laboratory, University of Nevada, Las Vegas, Las Vegas, Nevada 89154, United States*; orcid.org/0000-0003-1087-5815; Email: keith.lawler@unlv.edu

Linn Leppert − *MESA+ Institute for Nanotechnology, University of Twente, Enschede 7500 AE, The Netherlands*; orcid.org/0000-0002-4361-4382; Email: l.leppert@utwente.nl

Carolin M. Sutter-Fella − *Molecular Foundry Division, Lawrence Berkeley National Laboratory, Berkeley, California 94710, United States*; orcid.org/0000-0002-7769-0869; Email: csutterfella@lbl.gov

Authors

Do-Kyoung Lee − *Nevada Extreme Conditions Laboratory, University of Nevada, Las Vegas, Las Vegas, Nevada 89154, United States; Molecular Foundry Division, Lawrence Berkeley National Laboratory, Berkeley, California 94710, United States*; orcid.org/0009-0006-8393-3069

Kostas Fykouras − *MESA+ Institute for Nanotechnology, University of Twente, Enschede 7500 AE, The Netherlands*

Tim Kodalle − *Molecular Foundry Division, Lawrence Berkeley National Laboratory, Berkeley, California 94710, United States; Advanced Light Source, Lawrence Berkeley National Laboratory, Berkeley, California 94710, United States*; orcid.org/0000-0002-8792-9669

Raphael F. Moral − *Nevada Extreme Conditions Laboratory, University of Nevada, Las Vegas, Las Vegas, Nevada 89154, United States; Molecular Foundry Division, Lawrence Berkeley National Laboratory, Berkeley, California 94710, United States*

Craig P. Schwartz − *Nevada Extreme Conditions Laboratory, University of Nevada, Las Vegas, Las Vegas, Nevada 89154, United States*; orcid.org/0000-0002-4149-2684

Complete contact information is available at: https://pubs.acs.org/10.1021/acsenergylett.4c03334

Author Contributions

#D.-K.L. and K.F. contributed equally. D.-K.L. developed the idea with continuous discussions and supervision by C.P.S., K.V.L., and C.M.S.-F. D.-K.L. designed the experiments. D.-K.L. and T.K. performed the GIWAXS measurements. GIWAXS analysis was done by D.-K.L., T.K., and R.F.M. supervised by N.T. and C.M.S.-F. D.-K.L. performed the UV Vis and XRD stability measurements. K.F., K.V.L., and L.L. developed, performed, and validated the calculations and simulations. D.-K.L. and C.M.S.-F. wrote the first manuscript draft followed by input from L.L. and K.V.L. All authors contributed feedback and commented on the manuscript.

Notes

The authors declare no competing financial interest.

ACKNOWLEDGMENTS

D.-K.L., C.P.S., K.V.L., and C.M.S.-F. acknowledge the Office of Science, Office of Basic Energy Sciences, of the U.S. Department of Energy under Contract Number DE-SC-0023355. T.K. acknowledges support from the U.S. Department of Energy (DOE), Office of Science, Office of Basic Energy Sciences, Materials Sciences and Engineering Division under contract no. DE-AC02-05-CH11231 (D2S2 program KCD2S2). R.F.M. acknowledges the support of Chemical Sciences, Geosciences and Biosciences Division, Office of Basic Energy Sciences, Office of Science, U.S. Department of Energy under DOE Grant no. DE-SC-0023355. Work at the Molecular Foundry was supported by the Office of Science, Office of Basic Energy Sciences, of the U.S. Department of Energy under Contract No. DE-AC02-05CH11231. Work at the Advanced Light Source (ALS) was done at beamline 12.3.2. The ALS is a DOE Office of Science User Facility under Contract No. DE-AC02-05CH11231. This research used resources of the National Energy Research Scientific Computing Center (NERSC), a Department of Energy Office of Science User Facility using NERSC awards BES-ERCAP0027372, BES-ERCAP0027444, and BES-ERCAP0027351. K.F. and L.L. acknowledge funding from the Dutch Research Council (NWO) under grant number OCENW.M20.337 and computational resources provided by the Dutch National Supercomputing Center Snellius supported by the SURF cooperative. K.F. and L.L. thank Menno Bokdam for insightful conversations about the machine-learning force fields. All the authors thank Seo-Ryeong Lee and Jin-Wook Lee for constructive discussions. We would also like to acknowledge Rohan Dhall's help with STEM measurements during the revision stage.

REFERENCES

(1) Al-Ashouri, A.; Köhnen, E.; Li, B.; Magomedov, A.; Hemple, H.; Caprioglio, P.; Márquez, J. A.; Vilches, A. B. M.; Kasparavicius, E.; Smith, J. A.; Phung, N.; Menzel, D.; Grischek, M.; Kegelmann, L.; Skroblin, D.; Gollwitzer, C.; Malinauskas, T.; Jošt, M.; Matic, G.; Rech, B.; Schlatmann, R.; Topič, M.; Korte, L.; Abate, A.; Stannowski, B.; Neher, D.; Stolterfoht, M.; Unold, T.; Getautis, V.; Alberecht, S. Monolithic perovskite/silicon tandem solar cell with > 29% efficiency by enhanced hole extraction. *Science* **2020**, *370* (6522), 1300−1309.

(2) Kim, J. Y.; Lee, J.-W.; Jung, H. S.; Shin, H.; Park, N.-G. High-Efficiency Perovskite Solar Cells. *Chem. Rev.* **2020**, *120*, 7867−7918.

(3) Lee, D.-K.; Park, N.-G. Additive engineering for highly efficient and stable perovskite solar cells. *Appl. Phys. Rev.* **2023**, *10*, No. 011308.

(4) Wu, S.; Chen, Z.; Yip, H.-L.; Jen, A. K.-Y. The evolution and future of metal halide perovskite-based optoelectronic devices. *Matter* **2021**, *4*, 3814−3834.

(5) Ono, L. K.; Qi, Y.; Liu, S. Progress toward Stable Lead Halide Perovskite Solar Cells. *Joule* **2018**, *2*, 1961−1990.

(6) Akkerman, Q. A.; Rainò, G.; Kovalenko, M. V.; Manna, L. Genesis, challenges and opportunities for colloidal lead halide perovskite nanocrystals. *Nat. Mater.* **2018**, *17*, 394−405.

(7) Liu, D.; Luo, D.; Iqbal, A. N.; Orr, K. W. P.; Doherty, T. A. S.; Lu, Z.-H.; Stranks, S. D.; Zhang, W. Strain analysis and engineering in halide perovskite photovoltaics. *Nat. Mater.* **2021**, *20*, 1337−1346.

(8) Kim, G.; Min, H.; Lee, K. S.; Lee, D. Y.; Yoon, S. M.; Seok, S. I. Impact of strain relaxation on performance of α-formamidinium lead iodide perovskite solar cells. *Science* **2020**, *370*, 108−112.

(9) Zhao, J.; Deng, Y.; Wei, H.; Zheng, X.; Yu, Z.; Shao, Y.; Shield, J. E.; Huang, J. Strained hybrid perovskite thin films and their impact on the intrinsic stability of perovskite solar cells. *Sci. Adv.* **2017**, *3* (11), No. eaao5616.

(10) Yang, B.; Bogachuk, D.; Suo, J.; Wagner, L.; Kim, H.; Lim, J.; Hinsch, A.; Boschloo, G.; Nazeeruddin, M. K.; Hagfeldt, A. Strain effects on halide perovskite solar cells. *Chem. Soc. Rev.* **2022**, *51*, 7509−7530.

(11) Liu, Z.; Qiu, L.; Ono, L. K.; He, S.; Hu, Z.; Jiang, M.; Tong, G.; Wu, Z.; Jiang, Y.; Son, D.-Y.; Dang, Y.; Kazaoui, S.; Qi, Y. A holistic

approach to interface stabilization for efficient perovskite solar modules with over 2,000-h operational stability. *Nat. Energy* **2020**, *5*, 596−604.
(12) Wang, J. T.-W.; Wang, Z.; Pathak, S.; Zhang, W.; deQuilettes, D. W.; Wisnivesky-Rocca-Rivarola, F.; Huang, J.; Nayak, P. K.; Patel, J. B.; Yusof, H. A. M.; Vaynzof, Y.; Zhu, R.; Ramirez, I.; Zhang, J.; Ducati, C.; Grovenor, C.; Johnston, M. B.; Ginder, D. S.; Nicholas, R. J.; Snaith, H. J. Efficient perovskite solar cells by metal ion doping. *Energy Environ. Sci.* **2016**, *9*, 2892−2901.
(13) Saidaminov, M. I.; Kim, J.; Jain, A.; Quintero-Bermudez, R.; Tan, H.; Long, G.; Tan, F.; Johnston, A.; Zhao, Y.; Voznyy, O.; Sargent, E. H. Suppression of atomic vacancies via incorporation of isovalent small ions to increase the stability of halide perovskite solar cells in ambient air. *Nat. Energy* **2018**, *3*, 648−654.
(14) Aristidou, N.; Eames, C.; Sanchez-Molina, I.; Bu, X.; Kosco, J.; Islam, M. S.; Haque, S. A. Fast oxygen diffusion and iodide defects mediate oxygen-induced degradation of perovskite solar cells. *Nat. Commun.* **2017**, *8*, 15218.
(15) Pols, M.; Vicent-Luna, J. M.; Filot, I.; van Duin, A. C. T.; Tao, S. Atomistic Insights Into the Degradation of Inorganic Halide Perovskite CsPbI3: A Reactive Force Field Molecular Dynamics Study. *J. Phys. Chem. Lett.* **2021**, *12*, 5519−5525.
(16) Biega, R.-I.; Leppert, L. Halogen vacancy migration at surfaces of CsPbBr3 perovskites: insights from density functional theory. *J. Phys. Energy* **2021**, *3*, No. 034017.
(17) Liu, X.; Zhang, Y.; Shi, L.; Liu, Z.; Huang, J.; Yun, J. S.; Zeng, Y.; Pu, A.; Sun, K.; Hameiri, Z.; Stride, J. A.; Seidel, J.; Green, M. A.; Hao, X. Exploring Inorganic Binary Alkaline Halide to Passivate Defects in Low-Temperature-Processed Planar-Structure Hybrid Perovskite Solar Cells. *Adv. Energy Mater.* **2018**, *8*, 1800138.
(18) Shard, A. G. Detection limits in XPS for more than 6000 binary systems using Al and Mg Kα X-rays. *Surf. Interface Anal.* **2014**, *46*, 175−185.
(19) Chen, W.; Zhou, Y.; Chen, G.; Wu, Y.; Tu, B.; Liu, F.-Z.; Huang, L.; Ching Ng, A. M.; Djurišić, A. B.; He, Z. Alkali Chlorides for the Suppression of the Interfacial Recombination in Inverted Planar Perovskite Solar Cells. *Adv. Energy Mater.* **2019**, *9* (19), 1803872.
(20) Abdi-Jalebi, M.; Andaji-Garmaroudi, Z.; Cacovich, S.; Stavrakas, C.; Philippe, B.; Richter, J. M.; Alsari, M.; Booker, E. P.; Hutter, E. M.; Pearson, A. J.; Lilliu, S.; Savenije, T. J.; Rensmo, H.; Divitini, G.; Ducati, C.; Friend, R. H.; Stranks, S. D. Maximizing and stabilizing luminescence from halide perovskites with potassium passivation. *Nature* **2018**, *555*, 497−501.
(21) Zhao, Y.; Tan, H.; Yuan, H.; Yang, Z.; Fan, J. Z.; Kim, J.; Voznyy, O.; Gong, X.; Quan, L. N.; Tan, C. S.; Hofkens, J.; Yu, D.; Zhao, Q.; Sargent, E. H. Perovskite seeding growth of formamidinium-lead-iodide-based perovskites for efficient and stable solar cells. *Nat. Commun.* **2018**, *9*, 1607.
(22) Lee, J.-W.; Lee, D.-K.; Jeong, D.-N.; Park, N.-G. Control of Crystal Growth toward Scalable Fabrication of Perovskite Solar Cells. *Adv. Funct. Mater.* **2019**, *29* (47), 1807047.
(23) Zhou, Y.; Game, O. S.; Pang, S.; Padture, N. P. Microstructures of Organometal Trihalide Perovskites for Solar Cells: Their Evolution from Solutions and Characterization. *J. Phys. Chem. Lett.* **2015**, *6* (23), 4827−4839.
(24) Jariwala, S.; Sun, H.; Adhyaksa, G. W.P.; Lof, A.; Muscarella, L. A.; Ehrler, B.; Garnett, E. C.; Ginger, D. S. Local Crystal Misorientation Influences Non-radiative Recombination in Halide Perovskites. *Joule* **2019**, *3* (12), 3048−3060.
(25) Luo, Q.; Jones, A. H. High-precision determination of residual stress of polycrystalline coatings using optimized XRD-sin2ψ technique. *ICMCTF 2010 Spec. Issue* **2010**, *205*, 1403−1408.
(26) Zhu, C.; Niu, X.; Fu, Y.; Li, N.; Hu, C.; Chen, Y.; He, X.; Na, G.; Liu, P.; Zai, H.; Ge, Y.; Lu, Y.; Ke, X.; Bai, Y.; Yang, S.; Chen, P.; Li, Y.; Sui, M.; Zhang, L.; Zhou, H.; Chen, Q. Strain engineering in perovskite solar cells and its impacts on carrier dynamics. *Nat. Commun.* **2019**, *10*, 815.
(27) Cao, J.; Tao, S. X.; Bobbert, P. A.; Wong, C.-P.; Zhao, N. Interstitial Occupancy by Extrinsic Alkali Cations in Perovskites and Its Impact on Ion Migration. *Adv. Mater.* **2018**, *30* (26), 1707350.
(28) Li, N.; Song, L.; Jia, Y.; Dong, Y.; Xie, F.; Wang, L.; Tao, S.; Zhao, N. Stabilizing Perovskite Light-Emitting Diodes by Incorporation of Binary Alkali Cations. *Adv. Mater.* **2020**, *32* (17), 1907786.
(29) Jinnouchi, R.; Lahnsteiner, J.; Karsai, F.; Kresse, G.; Bokdam, M. Phase Transitions of Hybrid Perovskites Simulated by Machine-Learning Force Fields Trained on the Fly with Bayesian Inference. *Phys. Rev. Lett.* **2019**, *122*, No. 225701.
(30) Xu, J.; Maxwell, A.; Song, Z.; Bati, A. S. R.; Chen, H.; Li, C.; Park, S. M.; Yan, Y.; Chen, B.; Sargent, E. H. The dynamic adsorption affinity of ligands is a surrogate for the passivation of surface defects. *Nat. Commun.* **2024**, *15*, 2035.
(31) Zheng, X.; Wu, C.; Jha, S. K.; Li, Z.; Zhu, K.; Priya, S. Improved Phase Stability of Formamidinium Lead Triiodide Perovskite by Strain Relaxation. *ACS Energy Lett.* **2016**, *1*, 1014−1020.
(32) Kunz, M.; Tamura, N.; Chen, K.; MacDowell, A. A.; Celestre, R. S.; Church, M. M.; Fakra, S.; Domning, E. E.; Glossinger, J. M.; Kirschman, J. L.; Morrison, G. Y.; Plate, D. W.; Smith, B. V.; Warwick, T.; Yashchuk, V. V.; Padmore, H. A.; Ustundag, E. A dedicated superbend x-ray microdiffraction beamline for materials, geo-, and environmental sciences at the advanced light source. *Rev. Sci. Instrum.* **2009**, *80*, No. 035108.
(33) Williamson, G. K.; Hall, W. H. X-ray line broadening from filed aluminium and wolfram. *Acta Metall.* **1953**, *1*, 22−31.
(34) Hoke, E. T.; Slotcavage, D. J.; Dohner, E. R.; Bowring, A. R.; Karunadasa, H. I.; McGehee, M. D. Reversible photo-induced trap formation in mixed-halide hybrid perovskites for photovoltaics. *Chem. Sci.* **2015**, *6*, 613−617.
(35) Halford, G. C.; Deng, Q.; Gomez, A.; Green, T.; Mankoff, J. M.; Belisle, R. A. Structural Dynamics of Metal Halide Perovskites during Photoinduced Halide Segregation. *ACS Appl. Mater. Interfaces* **2022**, *14*, 4335−4343.
(36) Steele, J. A.; Solano, E.; Hardy, D.; Dayton, D.; Ladd, D.; White, K.; Chen, P.; Hou, J.; Guang, H.; Saha, R. A.; Wang, L.; Gao, F.; Hofkens, J.; Roeffaers, M. B. J.; Chernyshov, D.; Toney, M. F. How to GIWAXS: Grazing Incidence Wide Angle X-Ray Scattering Applied to Metal Halide Perovskite Thin Films. *Adv. Energy Mater.* **2023**, *13*, 2300760.
(37) Sidhik, S.; Li, W.; Samani, M. H. K.; Zhang, H.; Wang, Y.; Hoffman, J.; Fehr, A. K.; Wong, M. S.; Katan, C.; Even, J.; Marciel, A. B.; Kanatzidis, M. G.; Blancon, J.-C.; Mohite, A. D. Memory Seeds Enable High Structural Phase Purity in 2D Perovskite Films for High-Efficiency Devices. *Adv. Mater.* **2021**, *33* (29), 2007176.
(38) Giannozzi, P.; Baroni, S.; Bonini, N.; Calandra, M.; Car, R.; Cavazzoni, C.; Ceresoli, D.; Chiarotti, G. L.; Cococcioni, M.; Dabo, I.; et al. QUANTUM ESPRESSO: a modular and open-source software project for quantum simulations of materials. *J. Phys.: Condens. Matter* **2009**, *21*, 395502.
(39) Giannozzi, P.; Andreussi, O.; Brumme, T.; Nardelli, M. B.; Calandra, M.; Car, R.; Cavazzoni, C.; Ceresoli, D.; Cococcioni, M.; et al. Advanced capabilities for materials modelling with Quantum ESPRESSO. *J. Phys.: Condens. Matter* **2017**, *29*, No. 465901.
(40) Perdew, J. P.; Burke, K.; Ernzerhof, M. Generalized Gradient Approximation Made Simple. *Phys. Rev. Lett.* **1996**, *77*, 3865−3868.
(41) Grimme, S.; Antony, J.; Ehrlich, S.; Krieg, H. A consistent and accurate ab initio parametrization of density functional dispersion correction (DFT-D) for the 94 elements H-Pu. *J. Chem. Phys.* **2010**, *132*, No. 154104.
(42) Grimme, S.; Ehrlich, S.; Goerigk, L. Effect of the damping function in dispersion corrected density functional theory. *J. Comput. Chem.* **2011**, *32*, 1456−1465.
(43) Prandini, G.; Marrazzo, A.; Castelli, I. E.; Mounet, N.; Marzari, N. Precision and efficiency in solid-state pseudopotential calculations. *Npj Comput. Mater.* **2018**, *4*, 72.
(44) Perdew, J. P.; Ruzsinszky, A.; Csonka, G. I.; Vydrov, O. A.; Scuseria, G. E.; Constantin, L. A.; Zhou, X.; Burke, K. Restoring the

https://doi.org/10.1021/acsenergylett.4c03334
ACS Energy Lett. 2025, 10, 1039−1049

Density-Gradient Expansion for Exchange in Solids and Surfaces. *Phys. Rev. Lett.* **2008**, *100*, No. 136406.
(45) Weller, M. T.; Weber, O. J.; Frost, J. M.; Walsh, A. Cubic Perovskite Structure of Black Formamidinium Lead Iodide, α-[HC(NH2)2]PbI3, at 298 K. *J. Phys. Chem. Lett.* **2015**, *6*, 3209−3212.
(46) Kresse, G.; Hafner, J. Ab initio molecular dynamics for liquid metals. *Phys. Rev. B* **1993**, *47*, 558−561.
(47) Kresse, G.; Furthmüller, J. Efficient iterative schemes for ab initio total-energy calculations using a plane-wave basis set. *Phys. Rev. B* **1996**, *54*, 11169−11186.
(48) Kresse, G.; Joubert, D. From ultrasoft pseudopotentials to the projector augmented-wave method. *Phys. Rev. B* **1999**, *59*, 1758−1775.
(49) Blöchl, P. E. Projector augmented-wave method. *Phys. Rev. B* **1994**, *50*, 17953−17979.
(50) Bartók, A. P.; Payne, M. C.; Kondor, R.; Csányi, G. Gaussian Approximation Potentials: The Accuracy of Quantum Mechanics, without the Electrons. *Phys. Rev. Lett.* **2010**, *104*, No. 136403.
(51) Bartók, A. P.; Kondor, R.; Csányi, G. On representing chemical environments. *Phys. Rev. B* **2013**, *87*, No. 184115.
(52) Fykouras, K.; Lahnsteiner, J.; Leupold, N.; Tinnemans, P.; Moos, R.; Panzer, F.; de Wijs, G. A.; Bokdam, M.; Grüninger, H.; Kentgens, A. P. M. Disorder to order: how halide mixing in MAPbI3−xBrx perovskites restricts MA dynamics. *J. Mater. Chem. A* **2023**, *11*, 4587−4597.

https://doi.org/10.1021/acsenergylett.4c03334
ACS Energy Lett. 2025, 10, 1039−1049